Inverse design strategies for buckling-guided assembly of 3D surfaces based on topology optimization

Zheng Xu [a,b], Zhichao Fan [c,d], Wenbo Pang [b,e], Yanyang Zi [a,*], Yihui Zhang [b,e,**]

[a] State Key Laboratory for Manufacturing and Systems Engineering, School of Mechanical Engineering, Xi'an Jiaotong University, Xi'an 710049, PR China
[b] AML, Department of Engineering Mechanics, Tsinghua University, Beijing 100084, PR China
[c] State Key Laboratory of Advanced Design and Manufacturing for Vehicle Body, Hunan University, Changsha, Hunan 410082, PR China
[d] College of Mechanical and Vehicle Engineering, Hunan University, Changsha, Hunan 410082, PR China
[e] Center for Flexible Electronics Technology, Tsinghua University, Beijing 100084, PR China

ARTICLE INFO

ABSTRACT

Complex three-dimensional (3D) mesostructures in advanced functional materials are attracting increasing interest, due to their widespread applications. Mechanically-guided 3D assembly through compressive buckling provides deterministic routes to a rich diversity of 3D mesostructures and microelectronic devices, with feature sizes ranging from sub-microscale to millimeter-scale. Existing studies established inverse design methods that map the target 3D geometry onto an unknown 2D precursor, but mainly focusing on filamentary ribbon-type geometries. Although strategies relying on spatial thickness variation of 2D precursors have been reported to achieve inverse design of 3D surfaces, this could lead to a lack of compatibility with well-developed planar fabrication technologies. In the framework of buckling-guided 3D assembly, this paper presents a computational method based on topology optimization to solve the inverse design problem of 3D surfaces from 2D precursors with uniform thickness distributions. Specifically, curvy ribbon components were exploited to discretize nondevelopable target surfaces, and then optimized to ensure that the assembled 3D surface has the best match with the target geometry. Combined computational and experimental studies over a dozen of elaborate examples, encompassing both the caged and even general target surfaces, demonstrate the effectiveness and applicability of the proposed method.

© 2021 Elsevier Ltd. All rights reserved.

1. Introduction

Three-dimensional (3D) mesostructures formed with high-performance materials have enabled important applications in diverse emerging areas, such as micro- and nano-electromechanical systems (MEMS and NEMS) [1–7], soft robotics [8–15], flexible electronics [16–25] and metamaterials [26–36]. Diverse technologies are now available for the manufacture of sophisticated 3D mesostructures [16,37–50]. Thereinto, a deterministic self-assembly approach guided by compressive buckling, as developed recently [51–55], has stimulated extensive interests, because of its versatile applicability to a broad range of length scales and excellent compatibility with mature planar fabrication technologies. By precisely controlling buckling deformations of patterned 2D precursors selectively bonded onto the pre-stretched elastomer substrate, this approach has enabled assembly of 3D mesostructures with a rich diversity of 3D configurations [56–60], as well as novel micro-devices with outstanding performances [24,61–65]. Existing studies concentrated on the theoretical/numerical prediction of 3D configurations based on the post-buckling analyses of predesigned 2D precursor structures under prescribed mechanical loadings, which can be regarded as a forward problem [66–71]. Meanwhile, to broaden the utility of the 3D assembly approach, a few strategies have been developed to solve the inverse design problem that determines the initial geometric parameters of 2D precursors and loading magnitudes for desired 3D structures [72–76]. For example, optimization methods with the genetic algorithm (GA) were reported to solve the inverse problem with a limited number of design variables [72,75], but such methods can only deal with filamentary ribbon-type geometries. In terms of the 3D assembly of curvy surface configurations, some very recent work [73,74] proposed analytic solutions to the inverse design problem, relying on the ideas of spatially varying stiffness and discretization-based approximation. However, these studies exploited non-uniform thickness distributions of initial

---

* Corresponding author.
** Corresponding author at: AML, Department of Engineering Mechanics, Tsinghua University, Beijing 100084, PR China.
E-mail addresses: ziyy@mail.xjtu.edu.cn (Y. Zi), yihuizhang@tsinghua.edu.cn (Y. Zhang).

planar structures to achieve accurately customized 3D geometries, which was not very compatible with well-established planar fabrication technologies.

In the framework of buckling-guided 3D assembly, this paper proposes a computational method based on topology optimization to achieve the inverse design of 3D surface structures assembled from 2D precursors with uniform thicknesses. By discretizing nondevelopable target 3D surfaces into a set of curvy ribbon components, we exploit an optimal choice of discretization obtained from the adaptive genetic algorithm (AGA) to reproduce desired 3D surfaces. Incorporating the width distribution in discretized ribbons as an additional design variable allows considerably enhanced computational accuracy for curvy surfaces like drum and semi-ellipsoid. In these cases, sandwich designs of 2D precursor structures enable the integrity of 3D surface reproduction. To realize surfaces with caged and more general shapes, two representative discretization strategies were introduced in the optimization approach, and its applicability has been demonstrated through >10 examples with combined computational and experimental results.

2. Inverse design to reproduce 3D surfaces with caged shapes

Most nondevelopable 3D surfaces cannot be created directly from the post-buckling process of flat sheets in the condition of small strains (e.g., <5%) for the constituent materials. Therefore, it is necessary to exploit the concept of discretization, in which the target 3D surface is divided into a set of ribbon-shaped components, to realize the shape reproduction through the buckling-guided assembly (Fig. 1(a)). Each ribbon component, whose thickness and width are much smaller than the length, can be modeled using the theory of Euler–Bernoulli beams. In this section, we first establish the basic mechanics model to obtain the 2D precursor configuration of the ribbon-framework structure discretized from the target surface. By setting the coordinate values of the points at the centroid lines of discretized ribbons as design variables, the inverse design method based on topology optimization is developed to reproduce centrally symmetric target surfaces in Section 2.2. Section 2.3 illustrates the implementation of finite element analyses (FEA) and experiments in this study. In Section 2.4, the results of the inverse design for centrally symmetric 3D surfaces are provided for the validation of the developed method. Section 2.5 introduces an improved method to further improve the accuracy and universality of the inverse design, by incorporating the ribbon width as an additional variable and optimizing the entire ribbon-framework structures discretized from the target surfaces.

2.1. Basic mechanics model

For centrally symmetric 3D surfaces, a typical class of surfaces with caged features, a discretization strategy along the circumferential direction can be adopted, where all discretized ribbon components are the same and connected through the central joint to form a ribbon-framework structure (Fig. 1(a)). In this case, by solving the inverse design problem for the discretized ribbon components, the whole centrally symmetric 3D target surface can be reproduced.

Let the YZ plane in the global coordinate system be the platform of the buckling-guided assembly. Consider a 3D hemispherical surface as the target surface whose analytical expression is given by

$$F(x, y, z) = x^2 + y^2 + z^2 - r^2 = 0, r > 0, x > 0, \tag{1}$$

as shown in Fig. 1(a). Figs. 1(b) and (c) illustrate the specific method for the inverse design of ribbon-shaped structures separated from the target surfaces. To begin with, we need to extract the topology of the target ribbon from the target surface, including the location of the centroid line (the red line) and the twist of the cross section. To simplify the numerical analysis, the whole configuration can be projected to the YZ plane, as shown in Fig. 1(b). The location of the centroid line for the target ribbon discretized from the target surface can be determined. For example, the two endpoints and the midpoint of the centroid line are $L(0, -r)$, $R(0, r)$ and $O(0, 0)$, respectively. By setting two additional points $A(y, z)$ and $B(-y, -z)$ in the centroid line, which are centrosymmetric about the midpoint, the function of the centroid line $\mathbf{r}(S) = (X(S), Y(S), Z(S))$ can be interpolated by these five sample points (using B-spline functions), where S denotes the arc-length coordinate of the centroid line.

As illustrated in Fig. 1(c), a local orthonormal coordinate system in terms of the Frenet frame $\mathbf{e}_i^*$ ($i = 1, 2, 3$) of the centroid line can be set up, where $\mathbf{e}_1^*$, $\mathbf{e}_2^*$ and $\mathbf{e}_3^*$ refer to the normal, binormal and tangent direction of the centroid axis, respectively. The Euler frame $\mathbf{e}_i$ ($i = 1, 2, 3$) of the curved beam can also be established, in which $\mathbf{e}_1$ and $\mathbf{e}_2$ are the orthogonal unit vectors along the principal axes of the cross section, and $\mathbf{e}_3$ is tangential to the centroid line, coinciding with $\mathbf{e}_3^*$. The vectors $\mathbf{e}_1$ and $\mathbf{e}_2$ are also the normal and tangent vectors of the 3D surface, respectively. The corresponding Euler frame of the initial planar ribbon is $\mathbf{E}_i$ ($i = 1, 2, 3$) instead. Thereby, the unit vector $\mathbf{e}_1^*$ and $\mathbf{e}_1$ can be easily obtained from the parametric function of the centroid line $\mathbf{r}(S)$ by

$$\mathbf{e}_1^* = \frac{\mathbf{r}''}{|\mathbf{r}''|} \tag{2}$$

and

$$\mathbf{e}_1 = -\frac{F'|_{\mathbf{r}=\mathbf{r}(S)}}{|F'|_{\mathbf{r}=\mathbf{r}(S)}|}, \tag{3}$$

where $F' = (F_x, F_y, F_z)$ is the first-order partial derivative of the analytical equation for the target surface. We introduce the angle rotating clockwise from $\mathbf{e}_1^*$ to $\mathbf{e}_1$ based on the right-handed screw rule as the torsional angle $\theta(S)$, which can be expressed by

$$\theta(S) = \arccos\left(\frac{\mathbf{e}_1^* \cdot \mathbf{e}_1}{|\mathbf{e}_1^*| |\mathbf{e}_1|}\right) = \arccos\left(\mathbf{e}_1^* \cdot \mathbf{e}_1\right), \tag{4}$$

to describe the twist of the cross section. Then, the Euler frame $\mathbf{e}_i$ can be related to the Frenet frame $\mathbf{e}_i^*$ by

$$\begin{pmatrix} \mathbf{e}_1 \\ \mathbf{e}_2 \\ \mathbf{e}_3 \end{pmatrix} = \begin{pmatrix} \cos\theta & \sin\theta & 0 \\ -\sin\theta & \cos\theta & 0 \\ 0 & 0 & 1 \end{pmatrix} \begin{pmatrix} \mathbf{e}_1^* \\ \mathbf{e}_2^* \\ \mathbf{e}_3^* \end{pmatrix}. \tag{5}$$

The curvature κ_1^* related with the Frenet frame of the centroid line can be calculated from the parametric equation $\mathbf{r}(S)$ by

$$\kappa_1^* = \left|\frac{d^2\mathbf{r}}{dS^2}\right| \geq 0. \tag{6}$$

Consequently, the bending curvature κ_1 of the target ribbon with respect to the direction of the sectional vector $\mathbf{e}_1$ can be determined from the curvature of the centroid line and the torsional angle by

$$\kappa_1 = -\frac{d\mathbf{e}_3}{dS} \cdot \mathbf{e}_2 = -\frac{d\mathbf{e}_3^*}{dS} \cdot \left(-\sin\theta \mathbf{e}_1^* + \cos\theta \mathbf{e}_2^*\right)$$
$$= \sin\theta \kappa_1^* \in \left[-\kappa_1^*, \kappa_1^*\right]. \tag{7}$$

For the slender ribbon whose thickness is much smaller than the width and the length, the compressive buckling process is mainly governed by out-of-plane bending and twisting deformations. The in-plane bending curvature is therefore assumed to be unchanged during the 3D assembly. As such, the curvature K_1 of the centroid
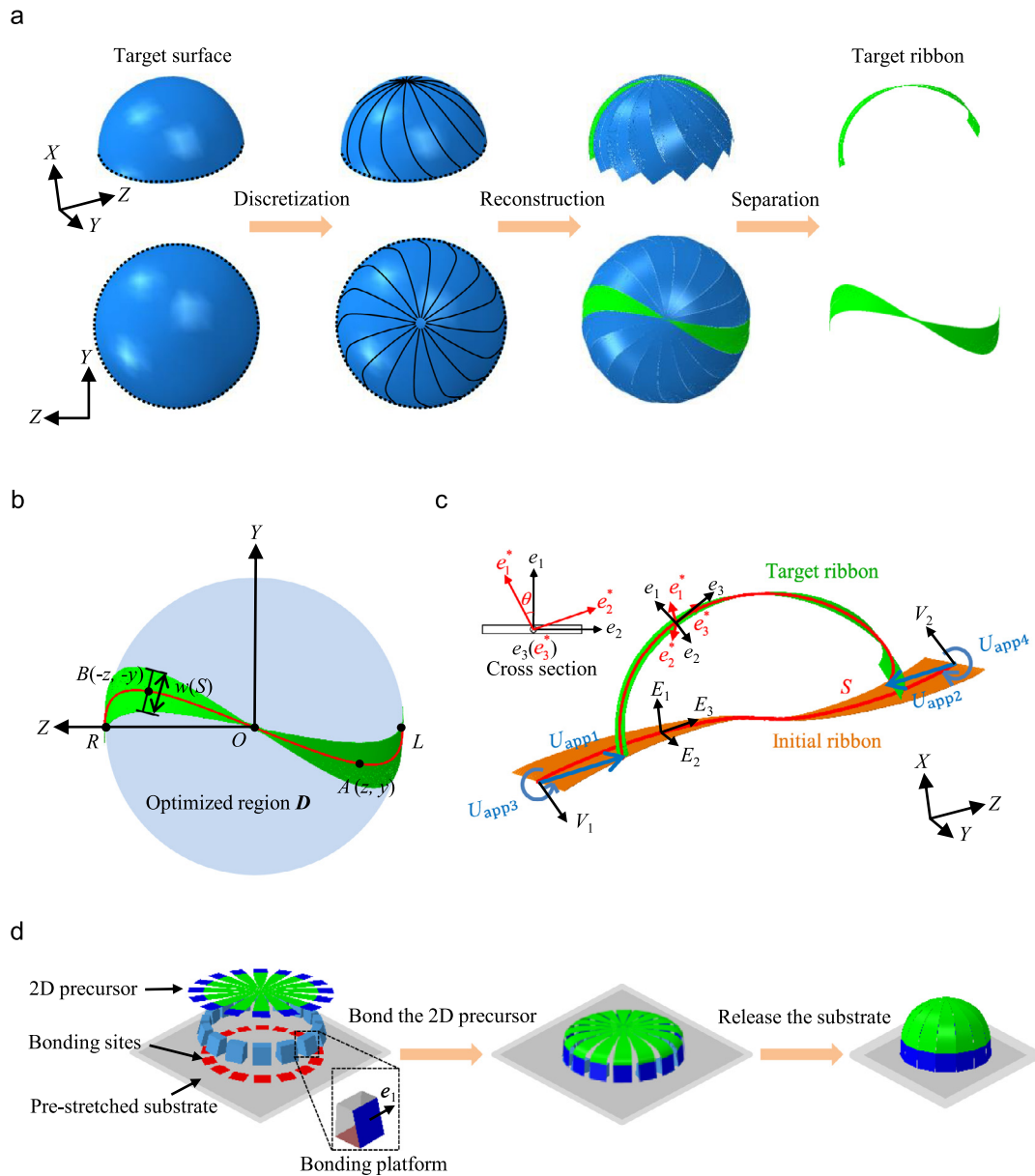
Fig. 1. Inverse design for centrally symmetric 3D surfaces. Schematic illustrations of (a) the discretization for nondevelopable centrally symmetric surfaces, (b) the topology optimization for one of the discretized ribbons, and (c) the mechanics model to analyze the ribbon structure assembled through compressive buckling under predefined loadings. (d) Fabrication procedures that transform the 2D precursor into desired 3D surface configuration, after release the pre-stretch in the substrate.

line of the initial 2D precursor is approximately equal to the bending curvature κ_1, and the centroid line of the planar ribbon can be determined consequently. Besides, the thickness of the ribbon is fixed as 1/900 of the arc length (Ls), and the width distribution can be solved accurately as

$$
w(S)
= \begin{cases}
\dfrac{\pi \sqrt{\left(Y^2(S) + Z^2(S)\right)}}{n}, & S \in \left[0, \dfrac{Ls}{2} - aLs\right] \cap \left[\dfrac{Ls}{2} + aLs, Ls\right] \\[3ex]
\dfrac{\pi \sqrt{\left(Y^2\left(\frac{Ls}{2} - aLs\right) + Z^2\left(\frac{Ls}{2} - aLs\right)\right)}}{n}, & S \in \left(\dfrac{Ls}{2} - aLs, \dfrac{Ls}{2} + aLs\right)
\end{cases},
$$

$$(8)$$

in which n refers to the number of ribbon components discretized from the target surface, and is set as 8 in the current study on the inverse design of 3D surfaces with caged shapes. The width of the ribbon component in the central area, with a distance of (aLs)

from the midpoint of the 2D precursor, keeps uniform to ensure connectivity of different ribbon components. To improve the accuracy of the inverse design, we introduce out-of-plane rotational loadings at each endpoint of ribbons in the 3D assembly, aside from in-plane displacement loadings. As shown in Fig. 1(c), the values of in-plane displacement at two ends, U_{app1} and U_{app2}, are determined as the distance of the corresponding ends between the target and the initial ribbon. The out-of-plane rotational angles, U_{app3} and U_{app4}, whose rotational axes are the V_1 and V_2 respectively, can be obtained according to their locations.

To this end, the initial planar ribbon configuration and the required loadings can be directly obtained, once the location of the centroid line for the target ribbon discretized from the target surface is determined. However, not all curved ribbons arbitrarily discretized from the target surface can be accurately formed through the buckling-guided assembly. To solve the inverse design problem of target 3D surfaces, our goal is to achieve the best match between the buckling configuration assembled through

prescribed loadings and the target ribbon-framework structure discretized from the desired surface, as defined by the centroid line and the twist of cross section.

2.2. Inverse design strategy based on topology optimization

The inverse design problem described in the current study can be formulated as a topology optimization problem to seek for the optimal layout of discretized ribbon component. According to the above mechanics model, the coordinate values of the two centrosymmetric points (A and B) can serve as the variables to be optimized within the optimized region $\boldsymbol{D}$ occupied by the target 3D surface, as shown in Fig. 1(b). We then introduce the relative coordinate error δ of the centroid line between the target and assembled configurations, which can be calculated in the least-squares form by

$$\delta = \frac{\sqrt{\sum_{k=1}^{m} \sum_{j=1}^{3} \left[C_j^{\text{result}}(S_k) - C_j^{\text{target}}(S_k) \right]^2}}{\sqrt{\sum_{k=1}^{m} \sum_{j=1}^{3} \left[C_j^{\text{target}}(S_k) - C_j^{\text{centroid}} \right]^2}}, \quad (9)$$

in which S_k ($k = 1, 2, \ldots, m$) refers to the arc-length coordinates of the node number k in the FEA; C_j ($j = 1, 2, 3$) is the coordinate component along the three axes (X, Y and Z) of the global coordinate system; C_j^{centroid} is the coordinate component of the centroid for the target surface in the YZ plane, which can be set as the intersection of the lines connecting two ends of all ribbons. For instance, C_j^{centroid} denotes the origin O for the target surface with a hemispherical shape. Since the optimization accuracy of the entire 3D surface depends on the match of both coordinates of the centroid line and torsional angles of the cross section, the objective function of such topology optimization problem can be defined with a simple linear weighted form as

$$\begin{aligned} \bar{\delta} &= \frac{\delta_C}{2} + \frac{\delta_{\boldsymbol{e}_3^*}}{4} + \frac{\delta_{\boldsymbol{e}_1^*}}{4} \\ &= \frac{\sqrt{\sum_{k=1}^{m} \sum_{j=1}^{3} \left[C_j^{\text{result}}(S_k) - C_j^{\text{target}}(S_k) \right]^2}}{2\sqrt{\sum_{k=1}^{m} \sum_{j=1}^{3} \left[C_j^{\text{target}}(S_k) - C_j^{\text{centroid}} \right]^2}} \\ &\quad + \frac{\sqrt{\sum_{i=1}^{v} \sum_{j=1}^{3} \left[e_{3j}^{*\text{result}}(S_i) - e_{3j}^{*\text{target}}(S_i) \right]^2}}{4\sqrt{\sum_{i=1}^{v} \sum_{j=1}^{3} \left[e_{3j}^{*\text{target}}(S_i) \right]^2}} \\ &\quad + \frac{\sqrt{\sum_{i=1}^{v} \sum_{j=1}^{3} \left[e_{1j}^{*\text{result}}(S_i) - e_{1j}^{*\text{target}}(S_i) \right]^2}}{4\sqrt{\sum_{i=1}^{v} \sum_{j=1}^{3} \left[e_{1j}^{*\text{target}}(S_i) \right]^2}}, \end{aligned} \quad (10)$$

where δ_C, $\delta_{\boldsymbol{e}_3^*}$ and $\delta_{\boldsymbol{e}_1^*}$ refer to relative errors of centroid line coordinates, vectors e_3^* and e_1^*, respectively [72]. Note that the weight coefficients can be altered according to the practical requirements. As such, the multiple objective problem can be converted to a single objective problem. Furthermore, we introduce the relative error of the torsional angle to compare the twist of the cross section between the target and optimized ribbon, which can be calculated by

$$\delta_\theta = \frac{\sum_{i=1}^{v} \left| \theta^{\text{result}}(S_i) - \theta^{\text{target}}(S_i) \right|}{\sum_{i=1}^{v} \theta^{\text{target}}(S_i)}, \quad (11)$$

where S_i ($i = 1, 2, \ldots, (v)$) refers to the arc-length coordinates of the sample nodes uniformly distributed on the ribbon in the FEA.

It should be pointed out that the AGA is suitable for the topology optimization of the inverse problem, owing to its general applicability and robustness in solving problems that are difficult to prescribe the analytical expression between the objective function and variables [77,78]. Compared with traditional GA, the improved AGA utilizes adaptive probabilities of crossover and mutation to enable a more rapid convergence to the global optimal solution. A modeling package for distributed evolutionary algorithms called DEAP [79] is used to implement the optimization process. 50 individuals per generation are set as a group of population to ensure the accuracy.

In summary, by assigning a minority of coordinate values of points (for discretization of the target surface) as the optimized variables and the weighted relative error as the objective function, the inverse design problem of the target 3D surfaces based on the topology optimization can be formulated as follows.

Find $P = (y_1, y_2, \ldots, y_n, z_1, z_2, \ldots, z_n)$

s.t. $y_n, z_n \in \boldsymbol{D}$

Minimize $\bar{\delta} = \frac{\delta_C}{2} + \frac{\delta_{\boldsymbol{e}_3^*}}{4} + \frac{\delta_{\boldsymbol{e}_1^*}}{4}$. $\quad (12)$

2.3. Implementation of FEA and experiments

This study combines numerical simulations and experimental measurements to illustrate the versatile utility of the proposed inverse design method. In the FEA, the commercial software ABAQUS with standard (implicit) solver was adopted to simulate the buckling-guided assembly process. Two-node beam elements (B31) were used for 2D precursor structures in polyimide (PI; elastic modulus = 2.5 GPa, and Poisson's ratio = 0.34), and refined meshes ensured the computational accuracy.

Fig. 1(d) illustrates the experimental process to transform the optimal 2D precursor into the desired 3D surface configuration. In our experiments, polyimide films (around 75 μm in thickness) patterned using the digital laser cutting served as 2D precursors solved from the inverse design. Small wedges (5 mm in thickness) fabricated by 3D printing were introduced as bonding platforms, such that the normal directions of the bonding surfaces are along the unit vectors $\boldsymbol{e}_1$ at the ends of ribbons, thereby exerting out-of-plane rotations during the assembly process. After adhering bonding platforms onto the pre-stretched silicone elastomer (around 2 mm in thickness, Dragon Skin) at the locations of predefined bonding sites, the 2D precursor can be transferred onto bonding platforms with covalent siloxane bonds. Releasing the substrate transforms the 2D precursor into 3D surface configuration.

2.4. Results of the inverse design for centrally symmetric 3D surfaces

We first consider the inverse design of a hemispherical surface, whose analytical expression is given by

$$x^2 + y^2 + z^2 = 25^2, x > 0. \quad (13)$$

As introduced in Section 2.1, completion of the inverse design for a single ribbon component can accomplish the reproduction of the entire surface with centrally symmetric shapes, since all discretized ribbons are identical. As such, there are only two design variables for this optimization problem. Fig. 2(a) presents the optimization histories of the inverse design starting from random initial values of the variables. After the evolution of 50 generations, the value of the objective function decreases to 4.00%, and the optimal discretized ribbon and the corresponding 2D precursor configuration are obtained. To intuitively illustrate the convergence and applicability of the optimization method, we extract the values of design variables at the first, second, fifth and last generations and compare the corresponding assembled ribbon-framework configurations with the target surface (Fig. 2(b)). As the generation number increases, the optimized surface configuration matches more closely with the target surface. Good agreements can also be observed with the quantitative comparison of both the coordinate components (based on FEA and experiment) from the top view (Fig. 2(c)) and the torsional
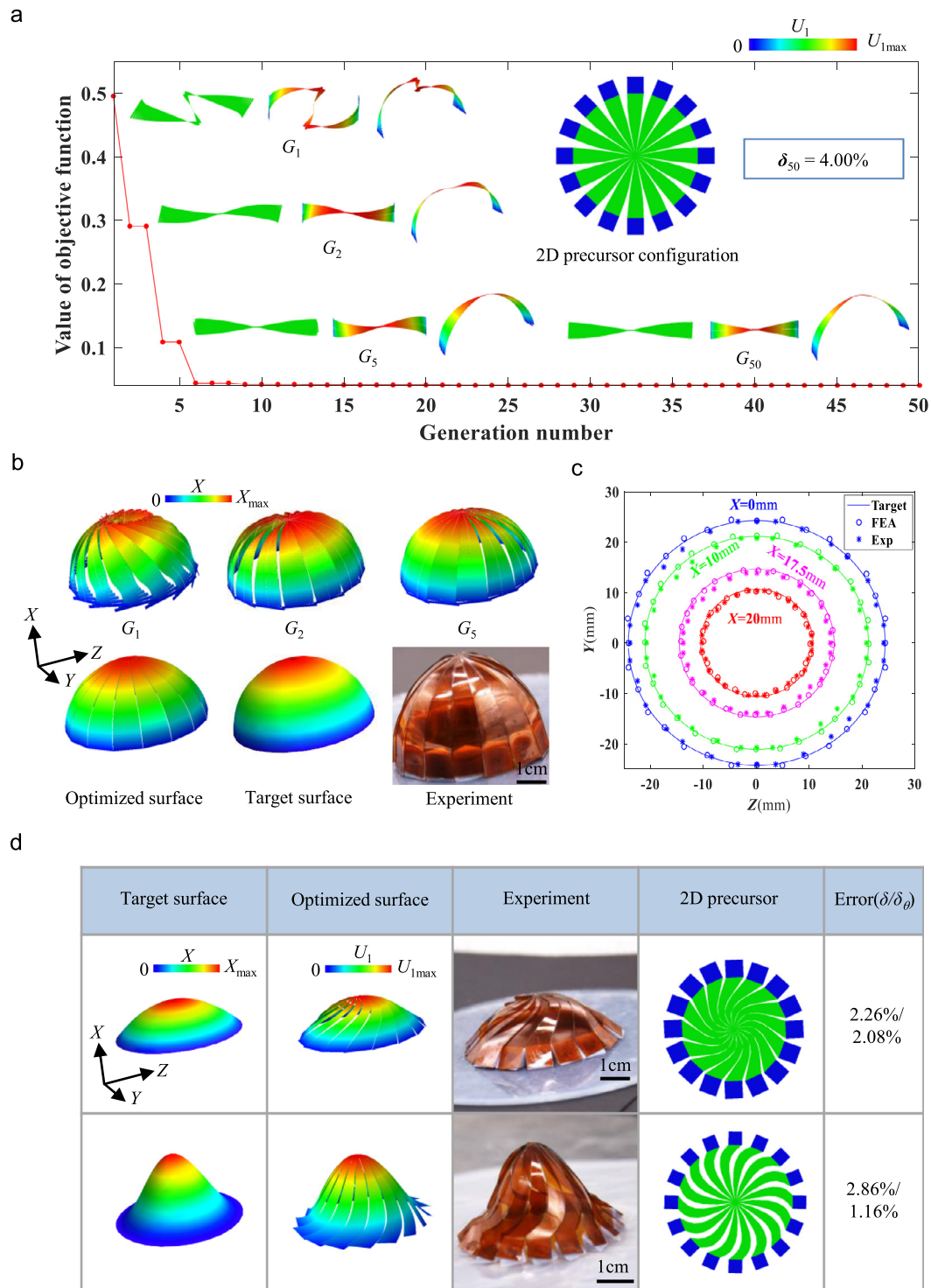
Fig. 2. Results of the inverse design for centrally symmetric 3D surfaces. (a) Optimization history of the inverse design for the hemispherical target surface, based on the adaptive genetic algorithm. G_i refers to the optimized 2D precursor configuration and the corresponding assembled structures from two views for one of the discretized ribbons up to the ith generation. (b) Comparison between assembled ribbon-framework configurations during the optimization process and the target hemispherical surface, along with the optical image in experiments. (c) Optimized and experimental results on the distribution of coordinate components for the hemispherical surface, in comparison to the target configuration. (d) Results of the inverse design for centrally symmetric 3D surfaces with the parabola-shaped and sinusoid-shaped generatrices. The color in the target surfaces and the optimized FEA configurations represents the magnitude of the coordinate value along the X axis and the out-of-plane displacement U_1, respectively. (For interpretation of the references to color in this figure legend, the reader is referred to the web version of this article.)

angles of the cross sections between the target and optimized discretized ribbons (Fig. S1).

Fig. 2(d) presents two additional examples of target 3D surfaces with centrally symmetric shapes, whose generatrices are

parabolic and sinusoidal curves, respectively. The analytical expressions of these two target surfaces are given by

$$2x + y^2 + z^2 = 1, x > 0 \tag{14}$$

and

$$2x - \cos\left(\pi\sqrt{y^2 + z^2}\right) = 1, x > 0. \tag{15}$$

These two 3D surfaces can also be well reproduced with the developed inverse design method. The obtained relative errors are very low (<3%) for both cases, as evidenced by the good agreements between target surfaces and experimentally assembled structures. It should be pointed out that the accuracy of the inverse design improves with the number of discretized ribbons increases, as demonstrated by optimization results for the target surface with the sinusoid-shaped generatrix (Fig. S2).

2.5. Improvement of the inverse design strategy

2.5.1. Optimization by introducing the widths of ribbons as additional variables

According to the previous studies [80–83], a nonuniform width distribution of the ribbon gives rise to the spatial change of bending and twisting stiffnesses, thereby affecting the shape of resulting 3D configurations during the assembly process. Based on the topology optimization, the inverse design can also incorporate the widths of ribbons as additional design variables, in order to enable improved accuracy of the inverse design strategy. For the inverse design of centrally symmetric 3D surfaces, the function of the normalized width $\overline{w}(S)$ can also be interpolated with five design variables $(\overline{w}_1, \overline{w}_2, 1, \overline{w}_2$ and $\overline{w}_1)$ using B-spline functions, where $\overline{w}_1$ and $\overline{w}_2$ are two additional variables of normalized widths. The range of these two width variables is set as [0.05, 1], considering that the ribbon-framework structure is discretized from the target surface and the width of the ribbon can only be decreased to avoid self-overlap. Then the function of decreased ribbon width $w'(S)$ can be obtained by

$$w'(S) = w(S)\,\overline{w}(S), \tag{16}$$

as shown in Fig. 3(a). To this end, the inverse design problem of the target centrally symmetric surface that incorporates the widths of the cross section as additional optimization variables can be given by

Find $P = (y_1, y_2, z_1, z_2, \overline{w}_1, \overline{w}_2)$

s.t. $y_1, y_2, z_1, z_2 \in \boldsymbol{D}, \overline{w}_1, \overline{w}_2 \in [0.05, 1]$

Minimize $\overline{\delta} = \dfrac{\delta_C}{2} + \dfrac{\delta_{\boldsymbol{e}_3^*}}{4} + \dfrac{\delta_{\boldsymbol{e}_1^*}}{4}.$ $\tag{17}$

Fig. 3(b) provides a solution to fill gaps between each ribbon component after the 3D assembly, owing to the decrease of ribbon widths. Here, a sandwich design of 2D precursor structures is adopted, where a layer of thin PI film (with initial widths in ribbon-framework structures) is transferred onto a layer of thick PI film (with decreased widths in ribbon-framework structures) with an adhesive layer. The thin film is much thinner (approximately 1/10) than the thick film, such that the shape of assembled configuration relies mainly on the optimized 2D precursor of the bottom thick layer. In the experiments, the thin and thick PI layers are ∼7.5 μm and ∼75 μm in thickness, respectively.

An example of the target surface with a drum shape, which can be analytically expressed by

$$9x + \left(y^2 + z^2\right)^2 = 9, x > 0, \tag{18}$$

is presented in Fig. 3(c) to illustrate the improved accuracy by additionally optimizing the widths of ribbon components. After 200 generations, the relative error of the optimization with variable width decreases to 5.24%, which is less than half of the relative error in the case of fixed width (without optimization). Through the comparison of assembled configurations, similar conclusions can be obtained that the optimized surface with decreased ribbon width matched more closely with the target drum surface than that with fixed width. Fig. 3(d) provides results of the inverse design for a drum surface, by exploiting sandwich precursor structures (based on FEA and experiment). These results demonstrate that the thin PI layer can not only eliminate the gaps between ribbon components to yield a complete 3D surface, but also have almost no influence on the shape of assembled configurations.

2.5.2. Inverse design of target surfaces with non-centrally symmetric caged shapes

For the class of non-centrally symmetric surfaces shown in Fig. 4(a), the discretized ribbons are not identical, and therefore, we cannot realize the reproduction merely through the inverse design for a single ribbon component. In this case, the entire ribbon-framework structure discretized from the target surface should be optimized. As an example, Fig. 4(b) illustrates the inverse design of target surfaces with more general caged shapes based on topology optimization. For one of the discretized ribbons, the functions of the edge lines $\boldsymbol{r}_1(S) = (X_1(S), Y_1(S), Z_1(S))$ and $\boldsymbol{r}_2(S) = (X_2(S), Y_2(S), Z_2(S))$ at two sides of the ribbon along the direction of the centroid line, namely, the cutting lines, can be interpolated by coordinate values of discrete sample points, (A_1, B_1, O, C_1, D_1) and (A_2, B_2, O, C_2, D_2), respectively. Here, (A_1, A_2) and (D_1, D_2) are at the two ends of the ribbon. Note that the number of sample points to be optimized can be decreased when the target surface has a certain degree of symmetry. For instance, we only need to consider two optimized sample points A_1 and B_1 to describe the ribbons along the Y or Z axis (i.e., the blue ribbons in Fig. 4(b)). As such, the function of the centroid line for each ribbon $\boldsymbol{r}(S) = (X(S), Y(S), Z(S))$ can be expressed in terms of the functions of its two cutting lines as

$$X(S) = \frac{X_1(S) + X_2(S)}{2}, Y(S) = \frac{Y_1(S) + Y_2(S)}{2},$$
$$Z(S) = \frac{Z_1(S) + Z_2(S)}{2}. \tag{19}$$

The function of torsional angle $\theta(S)$ can be obtained from the target surface, and the function of the width distribution $\boldsymbol{w}(S)$ can be calculated by as given in Box I.

It should be pointed out that the angle φ between two connecting ribbon components at the joint can be assumed unchanged during the assembly process, as shown in Fig. 4(b), since the deformations mainly occur at other locations. To this end, the improved inverse design problem to reproduce target surfaces with non-centrally symmetric caged shapes can be expressed by as given in Box II.

Box II in which $\overline{\boldsymbol{D}}$ represents the edge of the optimized region based on topology optimization, and the mean value of relative errors for all ribbons serves as the objective function of the optimization. In this case, the target surfaces are still discretized into framework structures with 8 ribbons.

Fig. 4(c) and Fig. S3 provide five examples to illustrate the utility of the optimization method. The analytical expressions of three target surfaces shown in Fig. 4(c) can be written as

$$\frac{x}{4} + \frac{y^2}{9} + \frac{z^2}{25} = 1, x > 0, \tag{22}$$
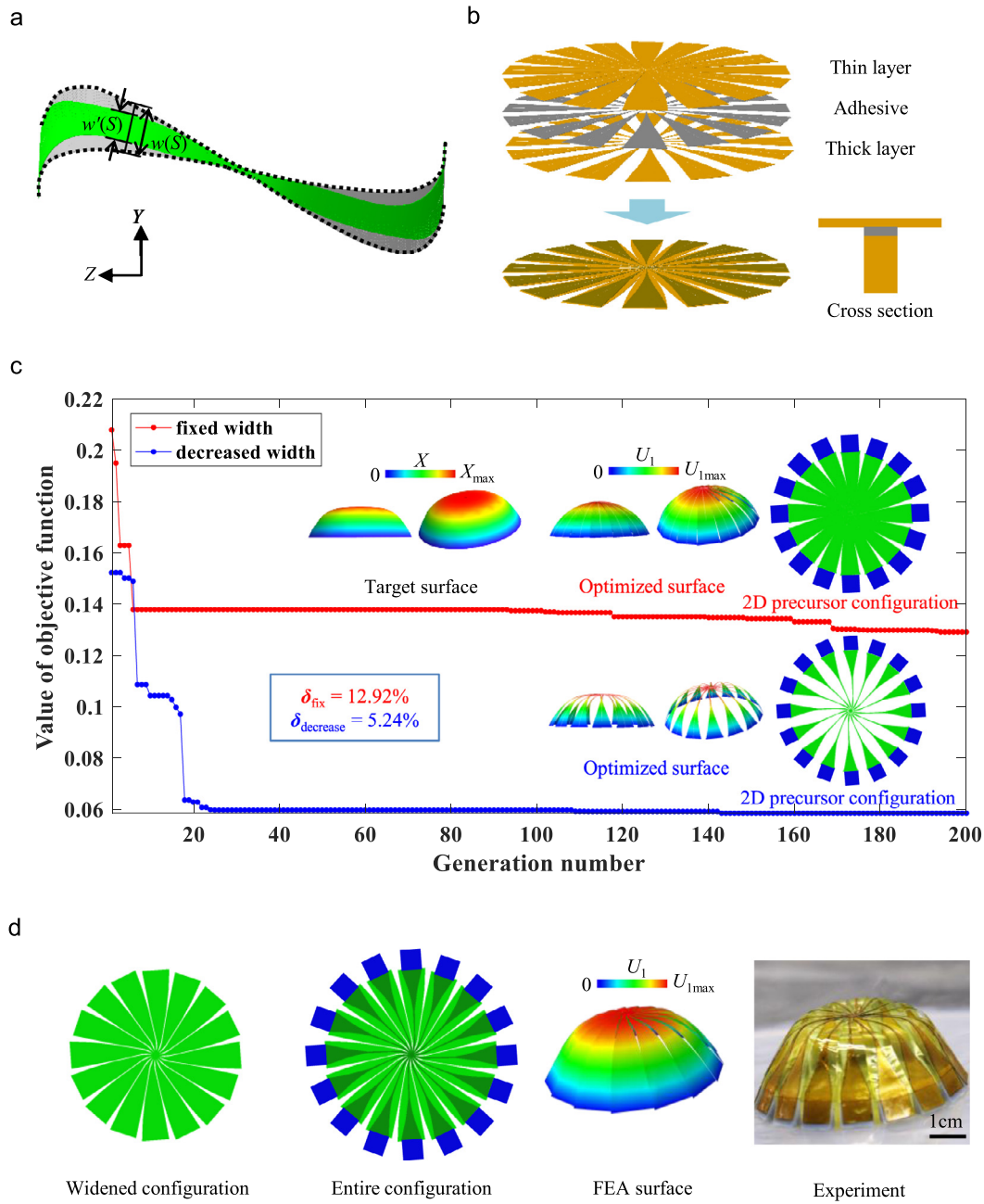
Fig. 3. Inverse design by introducing the ribbon width as an additional variable. Schematic illustrations of (a) the optimization for the width of the ribbon discretized from the centrally symmetric target surface and (b) the sandwich design that eliminates the gaps between assembled ribbons due to the decreased ribbon widths. (c) Comparisons of the optimization histories of the inverse design of the drum-shaped target surface between the cases with fixed and variable widths. (d) Results of the inverse design for the drum-shaped target surface with optimized widths, including the widened and whole configurations with the sandwich structure, as well as assembled configurations based on FEA and experiment. The color in the target surfaces and the optimized FEA configurations represents the magnitude of the coordinate value along the X axis and the out-of-plane displacement U_1, respectively.. (For interpretation of the references to color in this figure legend, the reader is referred to the web version of this article.)

$$w(S) = \begin{cases} \sqrt{(Y_1(S) - Y_2(S))^2 + (Z_1(S) - Z_2(S))^2}, S \in \left[0, \frac{Ls}{2} - aLs\right] \cap \left[\frac{Ls}{2} + aLs, Ls\right] \\ \sqrt{\left(Y_1\left(\frac{Ls}{2} - aLs\right) - Y_2\left(\frac{Ls}{2} - aLs\right)\right)^2 + \left(Z_1\left(\frac{Ls}{2} - aLs\right) - Z_2\left(\frac{Ls}{2} - aLs\right)\right)^2}, \\ S \in \left(\frac{Ls}{2} - aLs, \frac{Ls}{2} + aLs\right) \end{cases} \quad (20)$$

Box I.

a

b

c
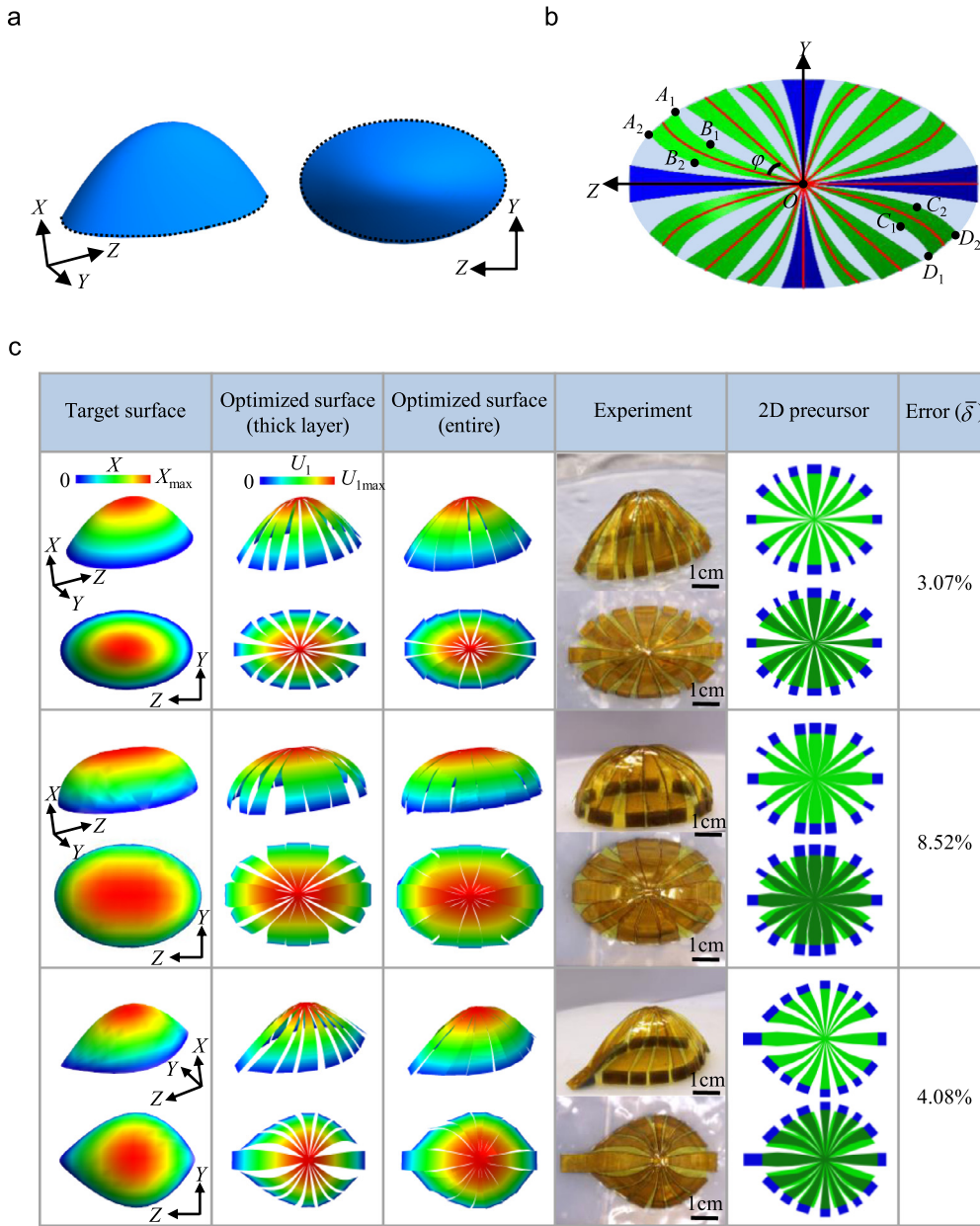
Fig. 4. Inverse design for general caged 3D surfaces. Schematic illustrations of (a) an example of general caged surfaces and (b) the optimization for the ribbon-framework structure discretized from the target surface. (c) Optimized and experimental results on the inverse design of three general caged 3D surfaces. The color in the target surfaces and the optimized FEA configurations represents the magnitude of the coordinate value along the X axis and the out-of-plane displacement U_1, respectively.. (For interpretation of the references to color in this figure legend, the reader is referred to the web version of this article.)

$$
\text{Find } P = \begin{bmatrix}
A_1^1(y_{11}, z_{11}), B_1^1(y_{21}, z_{21}), A_1^2(y_{12}, z_{12}), B_1^2(y_{22}, z_{22}), \dots, A_1^8(y_{18}, z_{18}), B_1^8(y_{28}, z_{28}), \\
A_2^1(y_{31}, z_{31}), B_2^1(y_{41}, z_{41}), A_2^2(y_{32}, z_{32}), B_2^2(y_{42}, z_{42}), \dots, A_2^8(y_{38}, z_{38}), B_2^8(y_{48}, z_{48}), \\
C_1^1(y_{51}, z_{51}), D_1^1(y_{61}, z_{61}), C_1^2(y_{52}, z_{52}), D_1^2(y_{62}, z_{62}), \dots, C_1^8(y_{58}, z_{58}), D_1^8(y_{68}, z_{68}), \\
C_2^1(y_{71}, z_{71}), D_2^1(y_{81}, z_{81}), C_2^2(y_{72}, z_{72}), D_2^2(y_{82}, z_{82}), \dots, C_2^8(y_{78}, z_{78}), D_2^8(y_{88}, z_{88}),
\end{bmatrix}
$$

s.t. $A_1^n, A_2^n, D_1^n, D_2^n \in \overline{\boldsymbol{D}}, B_1^n, B_2^n, C_1^n, C_2^n \in \boldsymbol{D}, n = 1, 2, \dots, 8$

$$
\text{Minimize } \overline{\delta} = \sum_{n=1}^{8} \left(\frac{\delta_C^n}{2} + \frac{\delta_{\boldsymbol{e}_3^*}^n}{4} + \frac{\delta_{\boldsymbol{e}_1^*}^n}{4} \right) / 8, \tag{21}
$$

Box II.

a

b
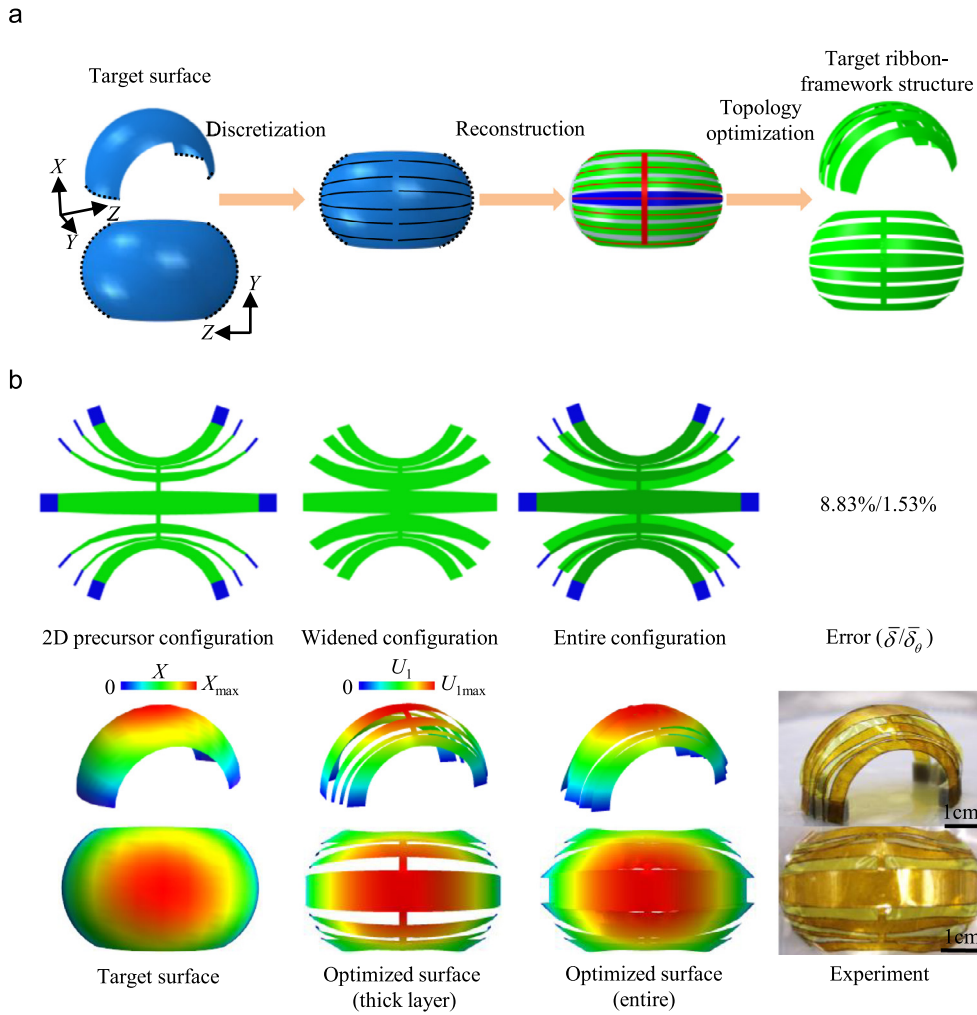
Fig. 5. Inverse design for 3D surfaces with more general shapes. (a) Schematic illustrations of the discretization for general nondevelopable surfaces. (b) Results of the inverse design for the arch-shaped target surface with optimized widths, including the widened and whole configurations with the sandwich structure, as well as assembled configurations based on FEA and experiment. The color in the target surfaces and the optimized FEA configurations represents the magnitude of the coordinate value along the X axis and the out-of-plane displacement U_1, respectively.. (For interpretation of the references to color in this figure legend, the reader is referred to the web version of this article.)

$$\begin{cases} x(\alpha, \beta) = \sqrt{0.5\cos(2\beta) + 1.5} \cos\alpha \sin\beta \\ y(\alpha, \beta) = \sin\alpha \\ z(\alpha, \beta) = \sqrt{0.5\cos(2\beta) + 1.5} \cos\alpha \cos\beta \end{cases},$$

$$\alpha \in \left[-\frac{\pi}{2}, \frac{\pi}{2}\right], \beta \in [0, \pi] \tag{23}$$

and

$$x^2 + y^2 - \frac{3}{4}\left[\frac{(z-1.5)^3}{9} - (z-1.5)\right]^2 = 0, x > 0. \tag{24}$$

These three target surfaces with non-centrally symmetric caged shapes can all be well reproduced using the developed topology optimization method, as shown by good agreements between the target and optimized surfaces, along with the experimentally assembled configurations. Moreover, Fig. S4 provides the optimization results of the inverse design with fixed ribbon width for the target semi-ellipsoidal surface for comparison with the results with decreased ribbon width shown in the first row of Fig. 4(c). The comparison further confirms that incorporating width distributions of discretized ribbons as additional design variables can greatly improve the accuracy.

3. Inverse design to reproduce 3D surfaces with more general shapes

In this section, we adopt the proposed method to achieve the inverse design of desired 3D surfaces that possess more general shapes. With an arch-shaped surface as an example, Fig. 5(a) illustrates a general discretization strategy inspired by CT scanning [74] for such target surfaces to solve the inverse design problem with topology optimization. The intersections of the target surface and the *YZ* plane (denoted by dotted lines in Fig. 5(a)) are regarded as the ends of discretized ribbons. Here, the target surface can be discretized into a ribbon-framework structure with an additional ribbon (denoted by red color) that connects the central points of each discretized ribbon. Similar to the inverse design of caged surfaces, the inverse design of target surfaces with general 3D shapes can be accomplished with the topology optimization of the entire ribbon-framework structures by optimizing the cutting lines.

Fig. 5(b) presents the results for the inverse design of the arch-shaped surface, whose analytical expression is given by

$$x^2 - \left(\sqrt{1-y^2} + 0.5\right)^2 + z^2 = 0, x > 0. \tag{25}$$

Fig. 6. Optimized and experimental results on the inverse design of general 3D surfaces. The color in the target surfaces and the optimized FEA configurations represents the magnitude of the coordinate value along the X axis and the out-of-plane displacement U_1, respectively.. (For interpretation of the references to color in this figure legend, the reader is referred to the web version of this article.)

Here, seven discretized ribbon components containing 70 sample points were adopted to reconstruct the arch-shaped surface, and the resulting structure shows good agreements with the target surface, as evidenced by the mean relative errors of both the coordinates of centroid lines and the torsional angles of cross sections for all discretized ribbons.

Fig. 6 provides four demonstrative examples to illustrate the powerful capability of the proposed method for the inverse design of general target surfaces, which can be described analytically by

$$
\begin{cases}
x(\alpha, \beta) = (\cos\alpha \sin\beta + 0.3\sin\beta)\left[(2\beta - \pi)^2/\pi^2 + 1\right] \\
y(\alpha, \beta) = \sin\alpha\left[(2\beta - \pi)^2/\pi^2 + 1\right] \\
z(\alpha, \beta) = (\cos\alpha \cos\beta + 0.3\cos\beta)\left[(2\beta - \pi)^2/\pi^2 + 1\right] \\
\quad \alpha \in \left[-\dfrac{\pi}{3}, \dfrac{\pi}{3}\right], \beta \in [0, \pi],
\end{cases}
$$

(26)

$$
\begin{cases}
x(\alpha, \beta) = \cos\alpha \sin\beta \\
y(\alpha, \beta) = \sin\alpha + 0.6\sin\beta - 0.3, \alpha \in \left[-\dfrac{\pi}{4}, \dfrac{\pi}{6}\right], \beta \in \left[\dfrac{\pi}{6}, \dfrac{5\pi}{6}\right], \\
z(\alpha, \beta) = \cos\alpha \cos\beta
\end{cases}
$$

(27)

$$
x + 2.1y^2 + 0.06yz + 0.9z^2 - 2.35y^4 + 1.6y^3z - 1.03y^2z^2 = 0.9,
$$
$$
y \in [-0.5, 0.5], z \in [-1.4, 1.4]
$$

(28)

and

$$
\begin{cases}
x(\alpha, t) = \dfrac{\sqrt{3}(3 - 2t)}{8}(1 - \sin\alpha) \\
y(\alpha, t) = \dfrac{2t - 3}{8}(1 + 3\sin\alpha) \quad , \alpha \in \left[\dfrac{\pi}{2}, \dfrac{5\pi}{2}\right], t \in [0, 1]. \\
z(\alpha, t) = \cos\alpha (t - 1.5)
\end{cases}
$$

(29)

Excluding the last example that adopts only 4 ribbon components in the discretization, the other three target surfaces are all discretized into 7 ribbon components. In all of these examples, the FEA and optical images of optimized assembled structures are always very similar to the target surfaces, as evidenced by the low relative error (<6%) between assembled and target configurations.

4. Conclusion

This work introduces a systematic study on the inverse design of 3D surface structures through the buckling-guided assembly.

By discretizing target 3D surfaces into ribbon-framework structures, an inverse design method based on topology optimization is developed to search for the optimal discretization strategy of the target surface. By taking into account spatially varying widths of discretized ribbons in the optimization, the accuracy of the inverse design is evidently improved, and target surfaces with general 3D shapes can be reproduced. Demonstrations across a dozen of complex 3D curvy surfaces with comparisons between the target and optimized configurations suggest a general applicability of the developed method.

Declaration of competing interest

The authors declare that they have no known competing financial interests or personal relationships that could have appeared to influence the work reported in this paper.

Acknowledgments

Appendix A. Supplementary data

Supplementary material related to this article can be found online at https://doi.org/10.1016/j.eml.2021.101582.

References

[1] R. Wang, W. Shen, W. Zhang, J. Song, N. Li, M. Liu, G. Zhang, C. Xue, W. Zhang, Design and implementation of a jellyfish otolith-inspired MEMS vector hydrophone for low-frequency detection, Microsyst. Nanoeng. 7 (1) (2021) http://dx.doi.org/10.1038/s41378-020-00227-w.

[2] B. Chen, W. Sun, J. Lu, J. Yang, Y. Chen, J. Zhou, Z. Suo, All-solid ionic eye, J. Appl. Mech. 88 (3) (2021) http://dx.doi.org/10.1115/1.4049198.

[3] R. Xu, H. Akay, S.G. Kim, Buckled MEMS beams for energy harvesting from low frequency vibrations, Research 2019 (2019) 1087946, http://dx.doi.org/10.34133/2019/1087946.

[4] H. Shim, K. Sim, F. Ershad, P. Yang, A. Thukral, Z. Rao, H.-J. Kim, Y. Liu, X. Wang, G. Gu, L. Gao, X. Wang, Y. Chai, C. Yu, Stretchable elastic synaptic transistors for neurologically integrated soft engineering systems, Sci. Adv. 5 (10) (2019) http://dx.doi.org/10.1126/sciadv.aax4961, eaax4961.

[5] Q. Liu, J. Huang, B. Xu, Evaporation-driven crumpling and assembling of two-dimensional (2D) materials: A rotational spring – mechanical slider model, J. Mech. Phys. Solids 133 (2019) http://dx.doi.org/10.1016/j.jmps.2019.103722.

[6] M. Han, H. Wang, Y. Yang, C. Liang, W. Bai, Z. Yan, H. Li, Y. Xue, X. Wang, B. Akar, H. Zhao, H. Luan, J. Lim, I. Kandela, G.A. Ameer, Y. Zhang, Y. Huang, J.A. Rogers, Three-dimensional piezoelectric polymer microsystems for vibrational energy harvesting, robotic interfaces and biomedical implants, Nat. Electron. 2 (1) (2019) 26–35, http://dx.doi.org/10.1038/s41928-018-0189-7.

[7] J. Rogers, Y. Huang, O.G. Schmidt, D.H. Gracias, Origami MEMS and NEMS, MRS Bull. 41 (2) (2016) 123–129, http://dx.doi.org/10.1557/mrs.2016.2.

[8] M. Zhu, O.G. Schmidt, Tiny robots and sensors need tiny batteries—Here's how to do it, Nature 589 (2021) 195–197, http://dx.doi.org/10.1038/d41586-021-00021-2.

[9] K. Yu, X. Ji, T. Yuan, Y. Cheng, J. Li, X. Hu, Z. Liu, X. Zhou, L. Fang, Robust jumping actuator with a shrimp-shell architecture, Adv. Mater. (2021) http://dx.doi.org/10.1002/adma.202104558, e2104558.

[10] Z. Zhai, Y. Wang, K. Lin, L. Wu, H. Jiang, In situ stiffness manipulation using elegant curved origami, Sci. Adv. 6 (47) (2020) http://dx.doi.org/10.1126/sciadv.abe2000, eabe2000.

[11] Y. Tang, Y. Chi, J. Sun, T.-H. Huang, O.H. Maghsoudi, A. Spence, J. Zhao, H. Su, J. Yin, Leveraging elastic instabilities for amplified performance: Spine-inspired high-speed and high-force soft robots, Sci. Adv. 6 (19) (2020) http://dx.doi.org/10.1126/sciadv.aaz6912, eaaz6912.

[12] Y. Chi, Y. Tang, H. Liu, J. Yin, Leveraging monostable and bistable pre-curved bilayer actuators for high-performance multitask soft robots, Adv. Mater. Technol. 5 (9) (2020) http://dx.doi.org/10.1002/admt.202000370.

[13] Y.F. Zhang, C.J.X. Ng, Z. Chen, W. Zhang, S. Panjwani, K. Kowsari, H.Y. Yang, Q. Ge, Miniature pneumatic actuators for soft robots by high-resolution multimaterial 3D printing, Adv. Mater. Technol. 4 (10) (2019) http://dx.doi.org/10.1002/admt.201900427.

[14] A. Kotikian, C. McMahan, E.C. Davidson, J.M. Muhammad, R. Weeks, D.C. Daraio, J.A. Lewis, Untethered soft robotic matter with passive control of shape morphing and propulsion, Sci. Robot. 4 (33) (2019) http://dx.doi.org/10.1126/scirobotics.aax7044, eaax7044.

[15] V. Slesarenko, S. Engelkemier, P. Galich, D. Vladimirsky, G. Klein, S. Rudykh, Strategies to control performance of 3D-printed cable-driven soft polymer actuators: from simple architectures to gripper prototype, Polymers 10 (8) (2018) http://dx.doi.org/10.3390/polym10080846.

[16] K. Kim, H.J. Kim, H. Zhang, W. Park, D. Meyer, M.K. Kim, B. Kim, H. Park, B. Xu, P. Kollbaum, B.W. Boudouris, C.H. Lee, All-printed stretchable corneal sensor on soft contact lenses for noninvasive and painless ocular electrodiagnosis, Nature Commun. 12 (1) (2021) 1544, http://dx.doi.org/10.1038/s41467-021-21916-8.

[17] J. Deng, H. Yuk, J. Wu, C.E. Varela, X. Chen, E.T. Roche, C.F. Guo, X. Zhao, Electrical bioadhesive interface for bioelectronics, Nat. Mater. 20 (2) (2021) 229–236, http://dx.doi.org/10.1038/s41563-020-00814-2.

[18] Z. Wang, L. Chen, Y. Chen, P. Liu, H. Duan, P. Cheng, 3D.Printed. Ultra-stretchable, Hyper-antifreezing conductive hydrogel for sensitive motion and electrophysiological signal monitoring, Research 2020 (2020) 1426078, http://dx.doi.org/10.34133/2020/1426078.

[19] C. Wang, C. Linghu, S. Nie, C. Li, Q. Lei, X. Tao, Y. Zeng, Y. Du, S. Zhang, K. Yu, H. Jin, W. Chen, J. Song, Programmable and scalable transfer printing with high reliability and efficiency for flexible inorganic electronics, Sci. Adv. 6 (25) (2020) http://dx.doi.org/10.1126/sciadv.abb2393, eabb2393.

[20] T. Sun, B. Zhou, Q. Zheng, L. Wang, W. Jiang, G.J. Snyder, Stretchable fabric generates electric power from woven thermoelectric fibers, Nature Commun. 11 (1) (2020) 572, http://dx.doi.org/10.1038/s41467-020-14399-6.

[21] F.R. Poblete, Z. Cui, Y. Liu, Y. Zhu, Stretching nanowires on a stretchable substrate: A method towards facile fracture testing and elastic strain engineering, Extreme Mech. Lett. 41 (2020) http://dx.doi.org/10.1016/j.eml.2020.101035.

[22] Q. Huang, Y. Zhu, Printing conductive nanomaterials for flexible and stretchable electronics: A review of materials, processes, and applications, Adv. Mater. Technol. 4 (5) (2019) http://dx.doi.org/10.1002/admt.201800546.

[23] B. Borgne, S. Liu, X. Morvan, S. Crand, R.A. Sporea, N. Lu, M. Harnois, Water transfer printing enhanced by water-induced pattern expansion: Toward large-area 3D electronics, Adv. Mater. Technol. 4 (4) (2019) http://dx.doi.org/10.1002/admt.201800600.

[24] H. Fu, K. Nan, W. Bai, W. Huang, K. Bai, L. Lu, C. Zhou, Y. Liu, F. Liu, J. Wang, M. Han, Z. Yan, H. Luan, Y. Zhang, Y. Zhang, J. Zhao, X. Cheng, M. Li, J.W. Lee, Y. Liu, D. Fang, X. Li, Y. Huang, Y. Zhang, J.A. Rogers, Morphable 3D mesostructures and microelectronic devices by multistable buckling mechanics, Nat. Mater. 17 (3) (2018) 268–276, http://dx.doi.org/10.1038/s41563-017-0011-3.

[25] Z. Jia, T. Li, Failure mechanics of a wrinkling thin film anode on a substrate under cyclic charging and discharging, Extreme Mech. Lett. 8 (2016) 273–282, http://dx.doi.org/10.1016/j.eml.2016.03.006.

[26] H. Zhang, J. Wu, D. Fang, Y. Zhang, Hierarchical mechanical metamaterials built with scalable tristable elements for ternary logic operation and amplitude modulation, Sci. Adv. 7 (9) (2021) http://dx.doi.org/10.1126/sciadv.abf1966, eabf1966.

[27] H. Wu, H. Zhang, C. Hao, Reconfigurable spiral underwater sound-absorbing metasurfaces, Extreme Mech. Lett. 47 (2021) http://dx.doi.org/10.1016/j.eml.2021.101361.

[28] J. Shi, H. Mofatteh, A. Mirabolghasemi, G. Desharnais, A. Akbarzadeh, Programmable multistable perforated shellular, Adv. Mater. (2021) http://dx.doi.org/10.1002/adma.202102423, e2102423.

[29] K. Liu, T. Tachi, G.H. Paulino, Bio-inspired origami metamaterials with metastable phases through mechanical phase transitions, J. Appl. Mech. 88 (9) (2021) http://dx.doi.org/10.1115/1.4050556.

[30] J. Liu, D. Yan, Y. Zhang, Mechanics of unusual soft network materials with rotatable structural nodes, J. Mech. Phys. Solids 146 (2021) http://dx.doi.org/10.1016/j.jmps.2020.104210.

[31] C. Liu, J. Shi, W. Zhao, X. Zhou, C. Ma, R. Peng, M. Wang, Z.H. Hang, X. Liu, J. Christensen, N.X. Fang, Y. Lai, Three-dimensional soundproof acoustic metacage, Phys. Rev. Lett. 127 (8) (2021) http://dx.doi.org/10.1103/PhysRevLett.127.084301.

[32] D. Yan, J. Chang, H. Zhang, J. Liu, H. Song, Z. Xue, F. Zhang, Y. Zhang, Soft three-dimensional network materials with rational bio-mimetic designs, Nature Commun. 11 (1) (2020) 1180, http://dx.doi.org/10.1038/s41467-020-14996-5.

[33] R. Wu, P.C.E. Roberts, S. Lyu, F. Zheng, C. Soutis, C. Diver, D. Zhou, L. Li, Z. Deng, Lightweight self-forming super-elastic mechanical metamaterials with adaptive stiffness, Adv. Funct. Mater. 31 (6) (2020) http://dx.doi.org/10.1002/adfm.202008252.

[34] B. Jenett, C. Cameron, F. Tourlomousis, A.P. Rubio, M. Ochalek, N. Gershenfeld, Discretely assembled mechanical metamaterials, Sci. Adv. 6 (47) (2020) http://dx.doi.org/10.1126/sciadv.abc9943, eabc9943.

[35] M. Lei, W. Hong, Z. Zhao, C. Hamel, M. Chen, H. Lu, H.J. Qi, 3D printing of auxetic metamaterials with digitally reprogrammable shape, ACS Appl. Mater. Interfaces 11 (25) (2019) 22768–22776, http://dx.doi.org/10.1021/acsami.9b06081.

[36] C. Coulais, E. Teomy, K. de Reus, Y. Shokef, M. van Hecke, Combinatorial design of textured mechanical metamaterials, Nature 535 (7613) (2016) 529–532, http://dx.doi.org/10.1038/nature18960.

[37] Z. Zhao, X.S. Zhang, Additive manufacturing of topology-optimized graded porous structures: An experimental study, Jom 73 (7) (2021) 2022–2030, http://dx.doi.org/10.1007/s11837-021-04705-y.

[38] Z. Shen, S. Li, Y. Xu, W. Yin, L. Zhang, X. Chen, Three-dimensional printed ultrabroadband terahertz metamaterial absorbers, Phys. Rev. Appl. 16 (1) (2021) http://dx.doi.org/10.1103/PhysRevApplied.16.014066.

[39] J.S. Cuellar, D. Plettenburg, A.A. Zadpoor, P. Breedveld, G. Smit, Design of a 3D-printed hand prosthesis featuring articulated bio-inspired fingers, Proc. Inst. Mech. Eng. H 235 (3) (2021) 336–345, http://dx.doi.org/10.1177/0954411920980889.

[40] Z. Zhang, B. Luce, C. Ma, B. Xie, N. Hu, Programmable origami-inspired cellular architected building blocks for flow-regulating adaptive weir, Extreme Mech. Lett. 40 (2020) http://dx.doi.org/10.1016/j.eml.2020.100974.

[41] Q. Zhang, X. Kuang, S. Weng, Z. Zhao, H. Chen, D. Fang, H.J. Qi, Rapid volatilization induced mechanically robust shape-morphing structures toward 4D printing, ACS Appl. Mater. Interfaces 12 (15) (2020) 17979–17987, http://dx.doi.org/10.1021/acsami.0c02038.

[42] Q. Liu, B. Xu, Solution evaporation-driven crumpling and assembling of large-accessible-space, high-mechanical-strength graphene/carbon nanotube composite nanoparticles, ACS Appl. Mater. Interfaces 12 (38) (2020) 43058–43064, http://dx.doi.org/10.1021/acsami.0c10532.

[43] Q. Guo, Y. Pan, J. Lin, G. Wan, B. Xu, N. Hua, C. Zheng, Y. Huang, Y. Mei, W. Chen, Z. Chen, Programmable 3D self-folding structures with strain engineering, Adv. Intell. Syst. 2 (12) (2020) http://dx.doi.org/10.1002/aisy.202000101.

[44] B. Xu, X. Zhang, Z. Tian, D. Han, X. Fan, Y. Chen, Z. Di, T. Qiu, Y. Mei, Microdroplet-guided intercalation and deterministic delamination towards intelligent rolling origami, Nature Commun. 10 (1) (2019) 5019, http://dx.doi.org/10.1038/s41467-019-13011-w.

[45] Y. Wang, L. Gao, S. Fan, W. Zhou, X. Li, Y. Lu, 3D printed micro-mechanical device (MMD) for in situ tensile testing of micro/nanowires, Extreme Mech. Lett. 33 (2019) http://dx.doi.org/10.1016/j.eml.2019.100575.

[46] K. Sim, S. Chen, Z. Li, Z. Rao, J. Liu, Y. Lu, S. Jang, F. Ershad, J. Chen, J. Xiao, C. Yu, Three-dimensional curvy electronics created using conformal additive stamp printing, Nat. Electron. 2 (10) (2019) 471–479, http://dx.doi.org/10.1038/s41928-019-0304-4.

[47] S.A. Nauroze, L.S. Novelino, M.M. Tentzeris, Correction for Nauroze, et al., Continuous-range tunable multilayer frequency-selective surfaces using origami and inkjet printing, Proc. Natl. Acad. Sci. USA 116 (22) (2019) 11074, http://dx.doi.org/10.1073/pnas.1907204116.

[48] D. Karnaushenko, T. Kang, O.G. Schmidt, Shapeable material technologies for 3D self-assembly of mesoscale electronics, Adv. Mater. Technol. 4 (4) (2019) http://dx.doi.org/10.1002/admt.201800692.

[49] Z. Song, C. Lv, M. Liang, V. Sanphuang, K. Wu, B. Chen, Z. Zhao, J. Bai, X. Wang, J.L. Volakis, L. Wang, X. He, Y. Yao, S. Tongay, H. Jiang, Microscale silicon origami, Small 12 (39) (2016) 5401–5406, http://dx.doi.org/10.1002/smll.201601947.

[50] H. Park, H. Cho, J. Kim, J.W. Bang, S. Seo, Y. Rahmawan, D.Y. Lee, K.Y. Suh, Multiscale transfer printing into recessed microwells and on curved surfaces via hierarchical perfluoropolyether stamps, Small 10 (1) (2014) 52–59, http://dx.doi.org/10.1002/smll.201300772.

[51] X. Wang, X. Guo, J. Ye, N. Zheng, P. Kohli, D. Choi, Y. Zhang, Z. Xie, Q. Zhang, H. Luan, K. Nan, B.H. Kim, Y. Xu, X. Shan, W. Bai, R. Sun, Z. Wang, H. Jang, F. Zhang, Y. Ma, Z. Xu, X. Feng, T. Xie, Y. Huang, Y. Zhang, J.A. Rogers, Freestanding 3D mesostructures, functional devices, and shape-programmable systems based on mechanically induced assembly with shape memory polymers, Adv. Mater. 31 (2) (2019) e1805615, http://dx.doi.org/10.1002/adma.201805615.

[52] H. Luan, X. Cheng, A. Wang, S. Zhao, K. Bai, H. Wang, W. Pang, Z. Xie, K. Li, F. Zhang, Y. Xue, Y. Huang, Y. Zhang, Design and fabrication of heterogeneous, deformable substrates for the mechanically guided 3D assembly, ACS Appl. Mater. Interfaces 11 (3) (2019) 3482–3492, http://dx.doi.org/10.1021/acsami.8b19187.

[53] X. Ning, X. Yu, H. Wang, R. Sun, R.E. Corman, H. Li, C.M. Lee, Y. Xue, A. Chempakasseril, Y. Yao, Z. Zhang, H. Luan, Z. Wang, W. Xia, X. Feng, R.H. Ewoldt, Y. Huang, Y. Zhang, J.A. Rogers, Mechanically active materials in three-dimensional mesostructures, Sci. Adv. 4 (9) (2018) http://dx.doi.org/10.1126/sciadv.aat8313, eaat8313.

[54] Y. Shi, F. Zhang, K. Nan, X. Wang, J. Wang, Y. Zhang, Y. Zhang, H. Luan, K.-C. Hwang, Y. Huang, J.A. Rogers, Y. Zhang, Plasticity-induced origami for assembly of three dimensional metallic structures guided by compressive buckling, Extreme Mech. Lett. 11 (2017) 105–110, http://dx.doi.org/10.1016/j.eml.2016.11.008.

[55] S. Xu, Z. Yan, K.-I. Jang, W. Huang, H. Fu, J. Kim, Z. Wei, M. Flavin, J. McCracken, R. Wang, A. Badea, Y. Liu, D. Xiao, G. Zhou, J. Lee, H.U. Chung, H. Cheng, W. Ren, A. Banks, X. Li, U. Paik, R.G. Nuzzo, Y. Huang, Y. Zhang, J.A. Rogers, Assembly of micro/nanomaterials into complex, three-dimensional architecturesby compressive buckling, Science 347 (6218) (2015) 154–159, http://dx.doi.org/10.1126/science.1260960.

[56] W. Pang, X. Cheng, H. Zhao, X. Guo, Z. Ji, G. Li, Y. Liang, Z. Xue, H. Song, F. Zhang, Z. Xu, L. Sang, W. Huang, T. Li, Y. Zhang, Electro-mechanically controlled assembly of reconfigurable 3D mesostructures and electronic devices based on dielectric elastomer platforms, Natl. Sci. Rev. 7 (2) (2020) 342–354, http://dx.doi.org/10.1093/nsr/nwz164.

[57] K. Bai, X. Cheng, Z. Xue, H. Song, L. Sang, F. Zhang, F. Liu, X. Luo, W. Huang, Y. Huang, Y. Zhang, Geometrically reconfigurable 3D mesostructures and electromagnetic devices through a rational bottom-up design strategy, Sci. Adv. 6 (30) (2020) http://dx.doi.org/10.1126/sciadv.abb7417, eabb7417.

[58] H. Zhao, K. Li, M. Han, F. Zhu, A. Vazquez-Guardado, P. Guo, Z. Xie, Y. Park, L. Chen, X. Wang, H. Luan, Y. Yang, H. Wang, C. Liang, Y. Xue, R.D. Schaller, D. Chanda, Y. Huang, Y. Zhang, J.A. Rogers, Buckling and twisting of advanced materials into morphable 3D mesostructures, Proc. Natl. Acad. Sci. USA 116 (27) (2019) 13239–13248, http://dx.doi.org/10.1073/pnas.1901193116.

[59] Y. Zhang, F. Zhang, Z. Yan, Q. Ma, X. Li, Y. Huang, J.A. Rogers, Printing, folding and assembly methods for forming 3D mesostructures in advanced materials, Nat. Rev. Mater. 2 (4) (2017) http://dx.doi.org/10.1038/natrevmats.2017.19.

[60] Y. Zhang, Z. Yan, K. Nan, D. Xiao, Y. Liu, H. Luan, H. Fu, X. Wang, Q. Yang, J. Wang, W. Ren, H. Si, F. Liu, L. Yang, H. Li, J. Wang, X. Guo, H. Luo, L. Wang, Y. Huang, J.A. Rogers, A mechanically driven form of kirigami as a route to 3D mesostructures in micro/nanomembranes, Proc. Natl. Acad. Sci. USA 112 (38) (2015) 11757–11764, http://dx.doi.org/10.1073/pnas.1515602112.

[61] Y. Ling, W. Pang, X. Li, S. Goswami, Z. Xu, D. Stroman, Y. Liu, Q. Fei, Y. Xu, G. Zhao, B. Sun, J. Xie, G. Huang, Y. Zhang, Z. Yan, Laser-induced graphene for electrothermally controlled, mechanically guided, 3D assembly and human-soft actuators interaction, Adv. Mater. 32 (17) (2020) e1908475, http://dx.doi.org/10.1002/adma.201908475.

[62] F. Zhang, F. Liu, Y. Zhang, Analyses of mechanically-assembled 3D spiral mesostructures with applications as tunable inductors, Sci. China Technol. Sci. 62 (2) (2018) 243–251, http://dx.doi.org/10.1007/s11431-018-9368-y.

[63] K. Nan, S.D. Kang, K. Li, K.J. Yu, F. Zhu, J. Wang, A.C. Dunn, C. Zhou, Z. Xie, M.T. Agne, H. Wang, H. Luan, Y. Zhang, Y. Huang, G.J. Snyder, J.A. Rogers, Compliant and stretchable thermoelectric coils for energy harvesting in miniature flexible devices, Sci. Adv. 4 (11) (2018) http://dx.doi.org/10.1126/sciadv.aau5849, eaau5849.

[64] W. Lee, Y. Liu, Y. Lee, B.K. Sharma, S.M. Shinde, S.D. Kim, K. Nan, Z. Yan, M. Han, Y. Huang, Y. Zhang, J.H. Ahn, J.A. Rogers, Two-dimensional materials in functional three-dimensional architectures with applications in photodetection and imaging, Nature Commun. 9 (1) (2018) 1417, http://dx.doi.org/10.1038/s41467-018-03870-0.

[65] B.H. Kim, F. Liu, Y. Yu, H. Jang, Z. Xie, K. Li, J. Lee, J.Y. Jeong, A. Ryu, Y. Lee, D.H. Kim, X. Wang, K. Lee, J.Y. Lee, S.M. Won, N. Oh, J. Kim, J.Y. Kim, S.J. Jeong, K.I. Jang, S. Lee, Y. Huang, Y. Zhang, J.A. Rogers, Mechanically guided post-assembly of 3D electronic systems, Adv. Funct. Mater. 28 (48) (2018) http://dx.doi.org/10.1002/adfm.201803149.

[66] Y. Liu, Z. Xu, K.C. Hwang, Y. Huang, Y. Zhang, Postbuckling analyses of frame mesostructures consisting of straight ribbons for mechanically guided three-dimensional assembly, Proc. Math. Phys. Eng. Sci. 475 (2225) (2019) 20190012, http://dx.doi.org/10.1098/rspa.2019.0012.

[67] Y. Liu, X. Wang, Y. Xu, Z. Xue, Y. Zhang, X. Ning, X. Cheng, Y. Xue, D. Lu, Q. Zhang, F. Zhang, J. Liu, X. Guo, K.C. Hwang, Y. Huang, J.A. Rogers, Y. Zhang, Harnessing the interface mechanics of hard films and soft substrates for 3D assembly by controlled buckling, Proc. Natl. Acad. Sci. USA 116 (31) (2019) 15368–15377, http://dx.doi.org/10.1073/pnas.1907732116.

[68] S. Li, M. Han, J.A. Rogers, Y. Zhang, Y. Huang, H. Wang, Mechanics of buckled serpentine structures formed via mechanics-guided, deterministic three-dimensional assembly, J. Mech. Phys. Solids 125 (2019) 736–748, http://dx.doi.org/10.1016/j.jmps.2019.01.019.

[69] F. Zhang, Z. Fan, Y. Zhang, A theoretical model of postbuckling in straight ribbons with engineered thickness distributions for three-dimensional assembly, Int. J. Solids Struct. 147 (2018) 254–271, http://dx.doi.org/10.1016/j.ijsolstr.2018.05.030.

[70] C. Lestringant, C. Maurini, A. Lazarus, B. Audoly, Buckling of an elastic ridge: Competition between wrinkles and creases, Phys. Rev. Lett. 118 (16) (2017) 165501, http://dx.doi.org/10.1103/PhysRevLett.118.165501.

[71] R. Al-Rashed, F. Lopez Jimenez, J. Marthelot, P.M. Reis, Buckling patterns in biaxially pre-stretched bilayer shells: wrinkles creases, folds and fracture-like ridges, Soft Matter 13 (43) (2017) 7969–7978, http://dx.doi.org/10.1039/c7sm01828b.

[72] Z. Xu, Z. Fan, Y. Zi, Y. Zhang, Y. Huang, An inverse design method of buckling-guided assembly for ribbon-type 3D structures, J. Appl. Mech. 87 (3) (2020) http://dx.doi.org/10.1115/1.4045367.

[73] M. Liu, L. Domino, D. Vella, Tapered elasticae as a route for axisymmetric morphing structures, Soft Matter 16 (33) (2020) 7739–7750, http://dx.doi.org/10.1039/d0sm00714e.

[74] Z. Fan, Y. Yang, F. Zhang, Z. Xu, H. Zhao, T. Wang, H. Song, Y. Huang, J.A. Rogers, Y. Zhang, Inverse design strategies for 3D surfaces formed by mechanically guided assembly, Adv. Mater. 32 (14) (2020) e1908424, http://dx.doi.org/10.1002/adma.201908424.

[75] Z. Xu, Z. Fan, H. Fu, Y. Liu, Y. Zi, Y. Huang, Y. Zhang, Optimization-based approach for the inverse design of ribbon-shaped three-dimensional structures assembled through compressive buckling, Phys. Rev. Appl. 11 (5) (2019) http://dx.doi.org/10.1103/PhysRevApplied.11.054053.

[76] R. Xue, R. Li, Z. Du, W. Zhang, Y. Zhu, Z. Sun, X. Guo, Kirigami pattern design of mechanically driven formation of complex 3D structures through topology optimization, Extreme Mech. Lett. 15 (2017) 139–144, http://dx.doi.org/10.1016/j.eml.2017.03.004.

[77] X.S. Zhang, H. Chi, G.H. Paulino, Adaptive multi-material topology optimization with hyperelastic materials under large deformations: A virtual element approach, Comput. Method. Appl. Mech. 370 (2020) http://dx.doi.org/10.1016/j.cma.2020.112976.

[78] M. Srinivas, L.M. Patnaik, Adaptive probabilities of crossover and mutation in genetic algorithms, IEEE Trans. Syst. Man Cybern. 24 (4) (1994) 656–667, http://dx.doi.org/10.1109/21.286385.

[79] F.A. Fortin, F.M. De Rainville, M.A. Gardner, M. Parizeau, C. Gagne, DEAP: Evolutionary algorithms made easy, J. Mach. Learn Res. 13 (2012) 2171–2175, http://dx.doi.org/10.1145/2330784.2330799.

[80] F. Liu, X. Jiang, X. Wang, L. Wang, Machine learning-based design and optimization of curved beams for multistable structures and metamaterials, Extreme Mech. Lett. 41 (2020) http://dx.doi.org/10.1016/j.eml.2020.101002.

[81] G. Luo, H. Fu, X. Cheng, K. Bai, L. Shi, X. He, J.A. Rogers, Y. Huang, Y. Zhang, Mechanics of bistable cross-shaped structures through loading-path controlled 3D assembly, J. Mech. Phys. Solids 129 (2019) 261–277, http://dx.doi.org/10.1016/j.jmps.2019.05.007.

[82] P. Jiao, W. Borchani, H. Hasni, N. Lajnef, Enhancement of quasi-static strain energy harvesters using non-uniform cross-section post-buckled beams, Smart Mater. Struct. 26 (8) (2017) http://dx.doi.org/10.1088/1361-665X/aa746e.

[83] Y. Huang, X.-F. Li, Buckling analysis of nonuniform and axially graded columns with varying flexural rigidity, J. Eng. Mech. 137 (1) (2011) 73–81, http://dx.doi.org/10.1061/(ASCE)EM.1943-7889.0000206.